The Astrophysical Journal, 747:65 (10pp), 2012 March 1 doi:10.1088/0004-637X/747/1/65

NONLINEAR FORCE-FREE MODELING OF A THREE-DIMENSIONAL SIGMOID OBSERVED ON THE SUN

S. Inoue[1,2], T. Magara[2], S. Watari[1], and G. S. Choe[2]
[1] National Institute of Information and Communications Technology (NICT), 4-2-1 Nukui-Kitamachi, Koganei, Tokyo 184-8795, Japan; inosato@khu.ac.kr
[2] School of Space Research, Kyung Hee University, Yongin, Gyeonggi-do 446-701, Republic of Korea
Received 2011 May 20; accepted 2011 December 20; published 2012 February 14

ABSTRACT

In this work, we analyze the characteristics of the three-dimensional magnetic structure of a sigmoid observed over an active region (AR 10930) and followed by X-class flares. This is accomplished by combining a nonlinear force-free field (NLFFF) model of a coronal magnetic field and the high-resolution vector-field measurement of a photospheric magnetic field by *Hinode*. The key findings of our analysis reveal that the value of the X-ray intensity associated with the sigmoid is more sensitive to the strength of the electric current rather than the twist of the field lines. The strong electric current flows along the magnetic field lines and composes the central part of the sigmoid, even though the twist of the field lines is weak in that region. On the other hand, the outer region (i.e., the elbow part) of the sigmoid is basically occupied by field lines of strong twist and weak current density. Consequently, weak X-ray emission is observed. As the initial Ca ii illumination basically occurs from the central part of the sigmoid, this region plays an important role in determining the onset mechanism of the flare despite its weak twisted field-line configuration. We also compare our results with the magnetohydrodynamic simulation for the formation of a sigmoid. Although the estimated values of the twist from the simulation are found to be a little higher than the values obtained from the NLFFF, we find that the field-line configurations generated by the simulation and NLFFF are remarkably analogous as long as we deal with the lower coronal region.

Key words: magnetic fields – Sun: flares – Sun: magnetic topology

Online-only material: color figures

1. INTRODUCTION

Sigmoids are observed either as an S or as an inverse of S-shaped structures with an enhanced value of the soft X-ray emission in the solar corona. It is believed that these structures are often a precursor for the big cusp-shaped flares (Tsuneta et al. 1992) or coronal mass ejections (e.g., Canfield et al. 1999; Sterling & Hudson 1997). Although *Yohkoh*/SXT clearly observed the S or reverse S-shaped structures, the internal magnetic configuration of sigmoids is still unknown. Recently, a new solar physics satellite, *Hinode* (Kosugi et al. 2007), observed the Sun with unprecedented resolution and will reveal several new features related to solar physics. From the soft X-ray observations of a sigmoid by *Hinode*, McKenzie & Canfield (2008) indicated that a sigmoid is not composed of a single X-ray loop, but consists of many loops. Many theoretical models have been proposed to explain the observed sigmoidal structures detected by *Yohkoh*/SXT and *Hinode*/XRT. For example, Moore et al. (2001) proposed that sigmoids are basically formed due to the shearing and twisting of the field lines, whereas its eruptions are governed by the magnetic reconnection in the middle sections of the sigmoids via the so-called tether-cutting reconnection process. In another perspective, Rust & Kumar (1996) and Rust & LaBonte (2005) suggested that sigmoidal structures are formed via kink instability in a twisted flux tube. However, arguments proposed by them were based on observational facts that the aspect ratio (width to length) of a bright sigmoid is close to the predicted aspect ratio of the kink instability developed in the flux tube. In another study, Leamon et al. (2003) argued that the twisting of the field lines that compose a sigmoid is not enough to produce kink instability. Besides these, in another theoretical model Titov & Démoulin (1999) indicated that two separatrix surfaces associated with two bald patches have the J-shaped structures through the flux rope emergence. Therefore, the sigmoid is regarded as the field lines near these separatrix surfaces. These apparently varied results make it important to investigate how the coronal magnetic field evolves and forms a sigmoid.

A series of numerical models have been extensively reported so far to explain the formation of the sigmoids.

Török & Kliem (2003) and Aulanier et al. (2010) showed that the twist motion of the sunspot could generate the sigmoidal current structure and field line structure under an eruptive flux tube. The kink instability is also considered as one of the possible processes for the formation of sigmoids. Matsumoto et al. (1998) presented the S-shaped structure formation from the kinked flux tube by using their numerical simulation. Kliem et al. (2004) showed that a transient sigmoid is formed by the field lines passing through the vertical current sheet under a kinked flux tube. Fan & Gibson (2004) indicated an S-shaped current sheet structure between an unstable flux tube and the pre-existing coronal field. The magnetic reconnection that occurred in this current sheet also plays an important role to brighten the sigmoidal structure. Inoue & Kusano (2006) also showed the formation of the S-shaped current sheet structure from a simple straight flux tube. Kusano (2005) proposed another model in which a sigmoid is formed by relaxation through the magnetic reconnection in the overlying field. The formation process as a result of an emerging flux was also reported in several studies. Magara & Longcope (2001) demonstrated that a sigmoid could be formed by the U-shaped field lines (U-loops) distributed below the axis of a twisted flux tube (see Figures 1(a) and (b)). They emerge close to the axis (Magara & Longcope 2003) and form either an S or inverse S-shaped structure depending on the initial magnetic helicity in the flux tube. These loops have a shallow dip so that they overcome the accumulation of mass at the dip which has a counter effect on emergence. After emerging, these shallow U-loops form a

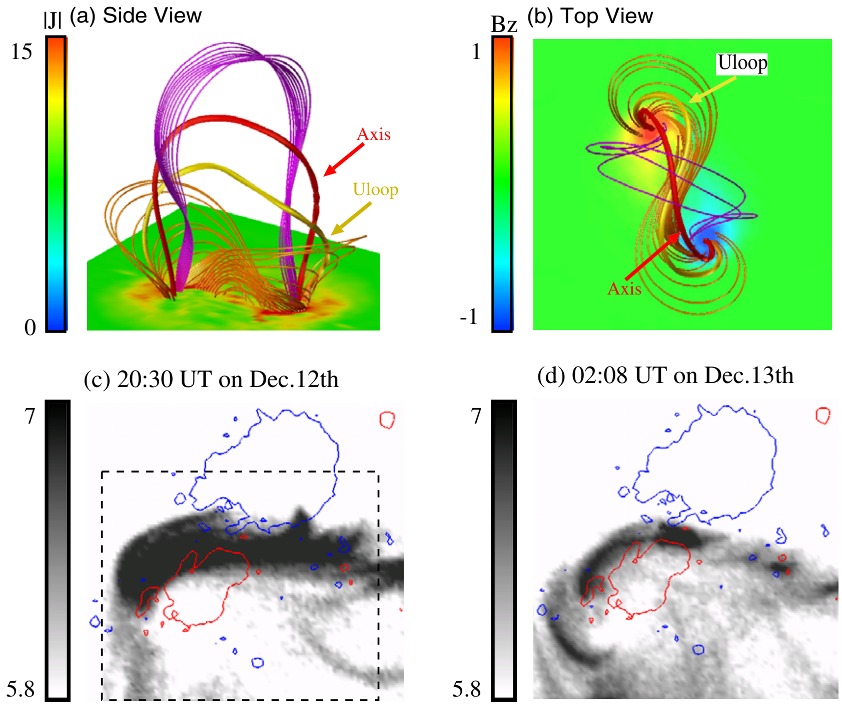

Figure 1. (a) and (b) are the side and top views of the field line structure as a result of a flux-emergence simulation (Magara 2004). Colored lines represent the magnetic field lines and the different colors (orange and purple) indicate the different twist number of the field lines (in a later discussion). The magnetic axis and U-loop are plotted by the thick red and yellow lines. The color planes in (a) and (b) show the current density $|\boldsymbol{J}|$ and normal component of the magnetic field, respectively. (c) and (d) show the X-ray intensity map obtained by *Hinode*/XRT between 5.8 and 7.0. The red and blue lines correspond to the contour of the normal component of the positive (790 G) and negative (−790 G) magnetic fields, respectively. (d) shows a state just before a flare occurs while (c) shows a state about 6 hr before the flare.

(A color version of this figure is available in the online journal.)

sheared arcade along the polarity inversion line because they have a strong axial component of the magnetic field. Magara & Longcope (2001) and later Magara (2004) explained that high current density tends to be distributed at the chromospheric footpoints of these shallow U-loops. Manchester et al. (2004) investigated the three-dimensional (3D) distribution of current density inside an emerging flux tube. They found an S-shaped current sheet structure surrounded by the dip of sheared and stretched field lines. Recently, the temporal development of a 3D distribution of current density inside an emerging flux tube has been reported in Archontis et al. (2009), where a comparison between the 3D distribution of the current density and soft X-ray image of a sigmoid is presented. They found that two J-like current structures are formed through the flux emergence and their coalesce produces the S-shaped sigmoid. They found that a sigmoid consists of many thin current sheets or layers causing the magnetic reconnection.

On the other hand, observations provide two-dimensional images of sigmoids, which actually just show a projected structure of a sigmoid. It is very important to reconstruct the 3D structure of a sigmoid from observations, and we have accomplished this by combining the nonlinear force-free field (NLFFF) model of the coronal field and the high-resolution vector-field measurement of photospheric field by *Hinode*. Recently, Su et al. (2009) and Savcheva & van Ballegooijen (2009) applied NLFFF reconstruction to the vector field obtained by *Hinode* and mentioned that the reconstructed field lines capture the structure of the intense soft X-ray emissions well. Their results indicated that NLFFF extrapolation is a strong tool to clarify a 3D magnetic structure.

In this study, we applied the NLFFF model to a sigmoid formed before an X3.4 class flare occurred in the solar active region (AR) NOAA 10930 to understand the detailed 3D structure and to establish a relation between the sigmoid and twisted field lines or field-aligned current in the chromosphere. Several authors have already applied the NLFFF extrapolation to AR 10930 and investigated before and after the flare (Schrijver et al. 2008; Inoue et al. 2008), compared with the observations (He et al. 2011; Inoue & Morikawa 2011; Inoue et al. 2011). Unfortunately, the vector field was observed at 20:30 UT on December 12 about 6 hr before the flare onset. Therefore, we compared the NLFFF with X-ray image in the growth phase of a sigmoid (see Figures 1(c) and (d)). We report an analysis of a 3D sigmoidal structure using the NLFFF model on AR 10930 and provide an origin of the sigmoid.

The rest of this paper is constructed as follows. The data set and simulation method is described in Section 2. The result of the 3D analysis of AR 10930 is presented in Section 3. The comparison with the theoretical models is discussed in Section 4. Some important conclusions are summarized in Section 5.

2. NUMERICAL METHOD

We use a classical relaxation method to reconstruct the NLFFF in AR 10930. It is widely believed that a coronal magnetic field satisfies the force-free condition,

$$\nabla \times \boldsymbol{B} = \alpha \boldsymbol{B} \tag{1}$$

derived from a low-β approximation in the solar corona. The NLFFF is extrapolated from the photospheric field as a boundary value problem. Unfortunately, the photospheric field deviates from the low-β approximation and hence, the NLFFF extrapolation is not a perfect technique. Inoue & Morikawa (2011) and Inoue et al. (2011) demonstrated its applicability by investigating the relationship between the field

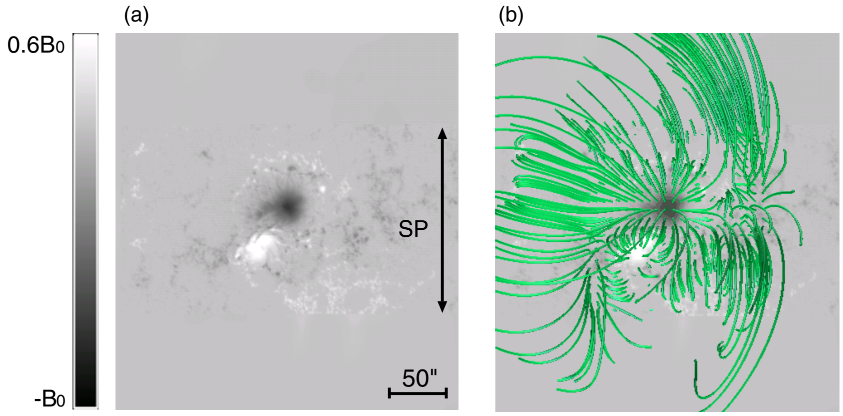

Figure 2. (a) The vector-field map where the *Hinode*/SP map is placed at the central region of the *SOHO*/MDI map. The gray color indicates the normal component of the magnetic field. (b) The potential field is calculated from the normal component of the magnetic field on all the boundaries. The green line indicates the magnetic field line.

(A color version of this figure is available in the online journal.)

lines' connectivity of NLFFF and Ca II or X-ray images obtained by the *Hinode* satellite.

The basic equations used in our study are written in dimensionless form as follows:

$$\frac{\partial \boldsymbol{v}}{\partial t} = -(\boldsymbol{v} \cdot \boldsymbol{\nabla})\boldsymbol{v} + \frac{1}{\rho}\boldsymbol{J} \times \boldsymbol{B} + \nu \boldsymbol{\nabla}^2 \boldsymbol{v}, \tag{2}$$

$$\frac{\partial \boldsymbol{B}}{\partial t} = \boldsymbol{\nabla} \times (\boldsymbol{v} \times \boldsymbol{B} - \eta \boldsymbol{J}) - \boldsymbol{\nabla}\phi, \tag{3}$$

$$\boldsymbol{J} = \boldsymbol{\nabla} \times \boldsymbol{B}, \tag{4}$$

and

$$\frac{\partial \phi}{\partial t} + c_h^2 \boldsymbol{\nabla} \cdot \boldsymbol{B} = -\frac{c_h^2}{c_p^2}\phi, \tag{5}$$

where $\boldsymbol{B}$ is the magnetic flux density, $\boldsymbol{v}$ is the velocity, $\boldsymbol{J}$ is the electric current density, ρ is the density, and ϕ is the potential function used to satisfy the divergence-free condition of the magnetic field. The length and magnetic field are normalized by $L_0 = 5.325 \times 10^9$ cm and $B_0 = 3957$ G. The density is given as a function of $|\boldsymbol{B}|$, expressed as $\rho = |\boldsymbol{B}|$. The non-dimensional viscosity ν is set as a constant (1.0×10^{-3}), and the non-dimensional resistivity η is given by the following function:

$$\eta = \eta_0 + \eta_1 \frac{|\boldsymbol{J} \times \boldsymbol{B}||\boldsymbol{v}|}{|\boldsymbol{B}|}, \tag{6}$$

where $\eta_0 = 5 \times 10^{-5}$, $\eta_1 = 1.0 \times 10^{-3}$ and the second term plays the role of acceleration toward the force-free condition. The other parameters c_h and c_p are fixed to 0.2 and 0.1, respectively.

The numerical scheme for this calculation is based on the Runge–Kutta–Gill method with fourth-order accuracy in time and a central difference method with second-order accuracy in space. The simulation domain is $(0, 0, 0) < (L_x, L_y, L_z) < (2.13, 2.34, 1.17)$ Mm in Cartesian coordinates, which is uniformly divided into $128 \times 128 \times 64$ grids. A vector-field map of photospheric magnetic field was obtained from the Solar Optical Telescope aboard *Hinode* (Kosugi et al. 2007), where we used the Milne–Eddington inversion of the Fe I lines at 630.15 nm and 630.25 nm to derive the vector information on the photospheric field. The transverse component of the magnetic field is determined using a method developed by the North West Research Associate (Leka et al. 2009). The *Hinode* vector-field map, with 125×64 pixels, is placed at the center of the bottom boundary of the simulation domain, reduced from the original data of 1000×512 pixels by applying 8×8 binning. The remaining area of the bottom boundary is covered by a *SOHO*/MDI map in Figure 2(a).

The bottom boundary condition is given by the hybrid map of *Hinode*/SP plus *SOHO*/MDI, while the other boundaries (top and laterals) are given by the potential field calculated from the synoptic map obtained from *SOHO*/MDI. The initial condition is given by the potential field in Figure 2(b), which is calculated from the normal component of the magnetic field on the all boundaries after conserving the total magnetic flux ($\int B_n dS = 0$) in the whole region, where the subscript n is the normal direction on the boundary surfaces. All the magnetic components are fixed to an initial condition and the velocity field is set to zero on all the boundaries. The Neumann-type boundary condition ($\partial_n \phi = 0$) is applied for the potential ϕ at all the boundaries, where ∂_n represents the derivative for normal direction on the surface.

3. RESULTS

3.1. The Three-dimensional Magnetic Structure of a Sigmoid

Figures 1(c) and (d) show the spatial relation between sunspots (red and blue contours) and sigmoids (background intensity map) observed in AR 10930. Red and blue contours indicate the positive and negative polarities while the background black and white map shows X-ray intensity obtained from *Hinode*/XRT between 5.8 and 7.0. From this two-dimensional image, we clearly see that the strong X-ray intensity lies on the neutral lines between the positive and negative sunspots.

Before 3D analysis, we first check how an extrapolated field satisfies the force-free condition. Figure 3(a) represents an iteration profile of $R = \int |\boldsymbol{J} \times \boldsymbol{B}|^2 dV$. This iteration is repeated about 2.0×10^6 times during which R decreases by about one order of magnitude from the initial value and the field is almost unchanged. Figure 3(b) plots the distribution of the force-free parameter α map at the final step. The horizontal axis is the value of the force-free α measured at one footpoint of each field line. The vertical axis is also the value of the force-free α at another footpoint of the field line. If an extrapolated field completely reproduces the force-free field, the all red dots

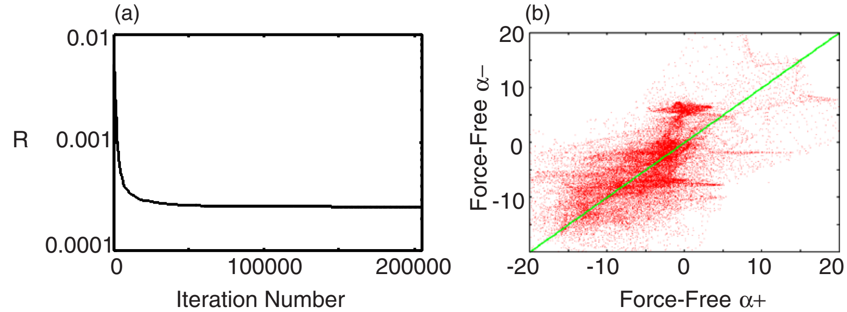

Figure 3. (a) An iteration profile of $R = \int |\boldsymbol{J} \times \boldsymbol{B}|^2 dV$ is plotted by the black solid line. (b) A distribution of the force-free α. The horizontal axis indicates the value of the force-free α on one footpoint of the field lines. The vertical axis is also the value of α on another footpoint of the field lines. If all red dots are on the green line ($y = x$), this indicates that the extrapolated field completely satisfies the force-free condition.

(A color version of this figure is available in the online journal.)

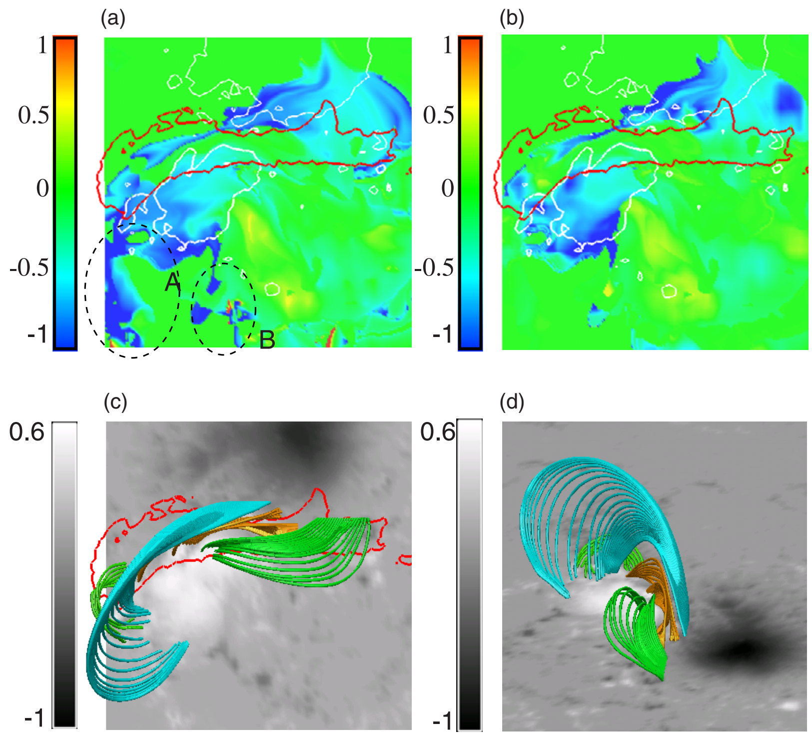

Figure 4. (a) and (b) show a photospheric map of the twist of the field line defined by the second and third terms of Equation (7). Positive and negative values represent the right- and left-handed twist of the field lines. The red contour indicates the X-ray intensity level of 6.8. (c) Magnetic field lines in different colors are plotted over the normal component of the magnetic field (gray-scale image). These colors indicate the different twist values; the orange, green, and blue represent $0 < |T_n| < 0.25$, $0.25 < |T_n| < 0.5$, and $0.5 < |T_n|$, respectively. (d) A side view of (c).

(A color version of this figure is available in the online journal.)

should be along the green line ($y = x$). Unfortunately, since the photosphere does not satisfy the force-free condition, it is rare that the force-free parameter α on both footpoints of each field line is the same.

Next, we compare the shape and X-ray emission of a sigmoid observed by *Hinode* with the 3D structure, which is focused on the twist number of each field line obtained from the NLFFF modeling. We introduce the twist of a field line showing how much a field line is twisted. The twist under the approximation of the force-free condition is defined as

$$T_n = \frac{1}{4\pi} \int \bar{\alpha} dl = \frac{1}{4\pi} \bar{\alpha} L, \tag{7}$$

where the line integral $\int dl$ is taken along the magnetic field line, L is the length of a field line from one footpoint to the other, and $\bar{\alpha}$ is the average of the force-free parameter $\boldsymbol{\nabla} \times \boldsymbol{B} = \alpha \boldsymbol{B}$ and defined as

$$\bar{\alpha} = \frac{1}{2}(\alpha_+ + \alpha_-), \tag{8}$$

where α_+ and α_- indicate the values of α at the two footpoints of a field line. The α_+ and α_- have different values in general because of the deviation of the actual magnetic field from a force-free state. In order to compensate for this, we use the average force-free parameter $\bar{\alpha}$ to represent the twist of a field line. In addition to these processes, we only focus on strong magnetic fields, where the normal component of magnetic field exceeds 30 G to avoid numerical error and $\alpha = 0$ is assumed in other areas. Finally, we operate the averaging over 3×3 cells on α_+ and α_-.

As the extrapolated field cannot completely satisfy the force-free condition, the second and third terms of Equation (7) are not exactly the same. Figures 4(a) and (b) show the distribution

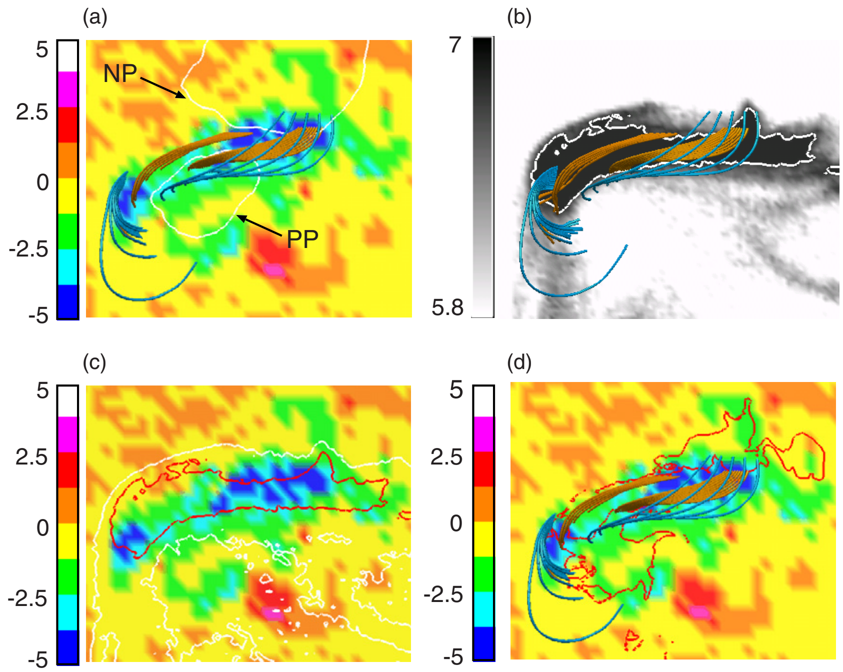

Figure 5. (a) The selected field lines are plotted over the color map of the field-aligned current density around the chromosphere (≈2000 km). The different colors of field lines indicate the different values of the field-aligned current density at the footpoints of these field lines on the negative polarity. The white contours named by PP and NP indicate the normal component of the magnetic field 600 G and −600 G, respectively. (b) The same field lines in (a) are plotted over the X-ray intensity map obtained from *Hinode*/XRT. (c) The X-ray intensities 6.8 and 5.8 by the red and white contours are plotted over a field-aligned current map. (d) Same as (a) and (c) except that the red contour indicates the twist of $|T_n| = 0.5$.

(A color version of this figure is available in the online journal.)

of the twist on the photosphere corresponding to the second and third terms of Equation (7), respectively. The X-ray intensity of value 6.8 is plotted in a red contour line. The display size corresponds to the dashed square in Figure 1(c). We found that twist distributions are similar at the strong magnetic field region, i.e., on sunspots, and the regions with strong twist appear in the dashed circle regions A and B only, as depicted in Figure 4(a). Because the third term in Equation (7) takes a small twist value, the large α value clearly appears on the field line except the bottom surface. However, this result seems to be inconsistent because the strong twist is formed by the motion of the sunspot with positive polarity in this AR, so the strong twist should appear on the sunspot region. Therefore, we adapt the twist formation due to the third term of Equation (7).

The twist distribution clearly shows that most of the field lines near the sigmoid have negative twist values, which correspond to the left-handed twist. This is consistent with the counterclockwise motion of sunspots with positive polarity. Figure 4(b) (also (a)) further shows that the most central part of the sigmoid is composed of the less twisted loops ($|T_n| < 0.5$), while several regions outside the red line are comprised of relatively more twisted loops ($0.5 < |T_n|$).

Figure 4(c) shows the 3D magnetic field lines. The different colors indicate the different twist values, which are classified into $0 < |Tn| < 0.25$ by the orange color, $0.25 < |Tn| < 0.5$ by green colors, and $0.5 < |Tn|$ by the blue color. Red contour lines are in the same format as given in Figure 4(b). Figure 4(d) represents the side view of Figure 4(c). These results indicate that a sigmoidal region is occupied by wide range twisted loops with different shapes; the core field especially is occupied by many fine structures with less twisted lines. Therefore, the sigmoid in this AR is not formed by a single magnetic loop but follows a much more complex structure. This result is consistent with data analysis (McKenzie & Canfield 2008) and numerical modelings (Magara 2004; Archontis et al. 2009).

3.2. Distribution of the Current Density

In this subsection, we also compare the NLFFF with the field-aligned current distribution in the chromosphere. Figure 5(a) shows a color map of the field-aligned current density:

$$J_{\mathrm{FAC}} = \boldsymbol{J} \cdot \frac{\boldsymbol{B}}{|\boldsymbol{B}|} \tag{9}$$

around the chromospheric height ($z \approx 2000$ km). The selected field lines are also plotted in different colors indicating different values of the field-aligned current density at the footpoints of these field lines on the negative polarity. The orange field lines belong to the range of the field-aligned current density over 3.75 and the blue field lines belong to the range from 1.25 to 2.5. The white solid lines, named PP and NP, represent the normal component of the magnetic field with a magnitude of 600 G and −600 G, respectively.

Figure 5(b) shows the same field lines as plotted in Figure 5(a), but over the X-ray intensity obtained by *Hinode*/XRT. Especially, the most strong X-ray intensity region is mainly occupied by the orange field lines. Figures 5(a) and (b) show that the footpoints of the field lines in the strong X-ray intensity region correspond to the region with the strong field-aligned current. We also plot the contours of the X-ray intensity of 6.8 (red contour line) and 5.8 (white contour line) over a field-aligned current map in Figure 5(c). Therefore, these results suggest that the strong field-aligned current flowing in the chromosphere produces X-ray emission via Joule heating of the plasma.

Figure 5(d) is the same as Figures 5(a) and (c) except that the red contour represents a twist of $|T_n| = 0.5$. From this result,

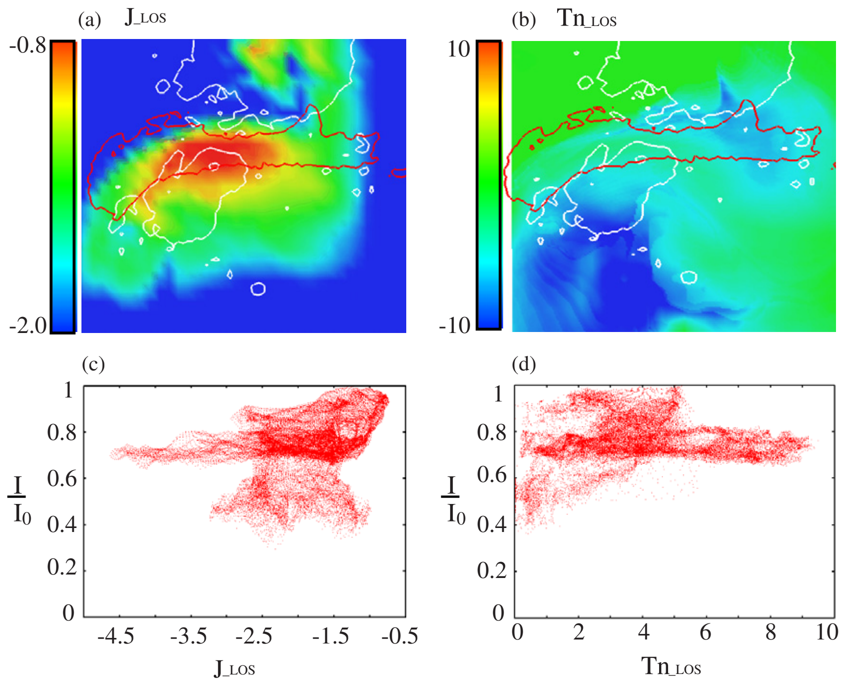

Figure 6. (a) Strong X-ray emission region (the red line) and the contour of the normal component of the positive (790 G) and negative (−790 G) magnetic fields (white lines) are plotted on the LOS-integrated current. (b) The same contour lines with (a) are plotted on the LOS-integrated twist. (c) and (d) represent the scatter plots for the X-ray emission (vertical axis) vs. LOS-integrated current and twist, respectively. I_0 corresponds to 7.84, which is the maximum value of X-ray intensity.

(A color version of this figure is available in the online journal.)

we found that the central part of the sigmoid is occupied by the weak twisted field lines in spite of the strong field-aligned current associated with it. On the other hand, the outer part of the sigmoid reveals the opposite behavior as compared to the central part.

3.3. An LOS-integrated Current/Twist versus a Sigmoid

We also compare the strong X-ray emission of a sigmoid with the current and twist integrated over the line of sight (LOS) to further strengthen the above results. The color maps in Figures 6(a) and (b) show the distributions of the logarithm of the LOS-integrated current ($J_{\rm LOS} = \log(\int |\boldsymbol{J}| dz)$) and LOS-integrated twist map ($Tn_{\rm LOS} = \int T_n dz$), respectively. The red and white lines indicate the strong X-ray region and the contour of the positive and negative polarities, which are in the same format as presented in Figure 4. From these results, it seems that the strong X-ray emission is related to the LOS-integrated current; on the other hand, the relation between the X-ray emission and LOS-integrated twist seems to run in the opposite direction, with strong X-ray emission from the weak LOS-twisted region.

Figures 6(c) and (d) show the scatter plots for the X-ray emission versus the LOS-integrated current/twist to show more quantitatively its behavior. The vertical axis represents the strength of the X-ray emission, which is normalized by the maximum value ($I_0 = 7.84$), and the horizontal axis represents the logarithm of the LOS-integrated current in (a) and the LOS-integrated twist in (b), respectively. It roughly seems that the current becomes stronger as the X-ray emission increases; on the other hand, in Figure 6(b), the maximum value of the X-ray emission reaches in the range between $Tn_{\rm LOS} = 2$ and $Tn_{\rm LOS} = 6$. Therefore, this result suggested that the strong X-ray emission is contributed from the strong current region in the chromosphere and lower corona.

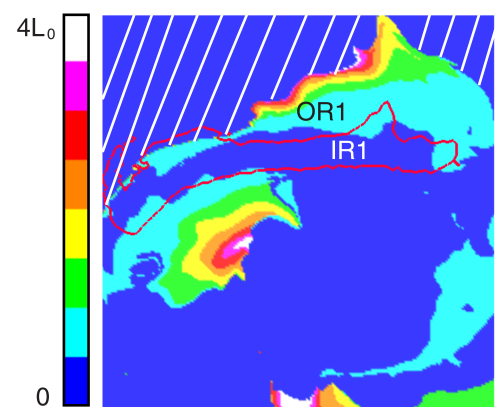

Figure 7. Field-line length is mapped on the photosphere in colors. The region plotted by the diagonal lines is occupied by the open field lines that are over the field of view. The red contour indicates an X-ray intensity level of 6.8. OR1 and IR1 represent the outer and inner regions of the red contour.

(A color version of this figure is available in the online journal.)

4. DISCUSSION

4.1. X-Ray Emission of a Sigmoid

In Figure 4(b) (also (a)), we found that the central part of a sigmoid shows strong X-ray emission in spite of a weak twist prevailing there. The reason for this could be explained in terms of the strong field-aligned current and length of the field line. We have already shown that the strong field-aligned current concentrated at the footpoints of the field lines occupying the central part of a sigmoid contributes to heating the plasma via dissipation of the current. Figure 7 shows the field-line length mapped on the photosphere. Regions marked by diagonal lines are occupied by the open field lines that are over the field of view in Figure 7. The surrounding region shown by the red

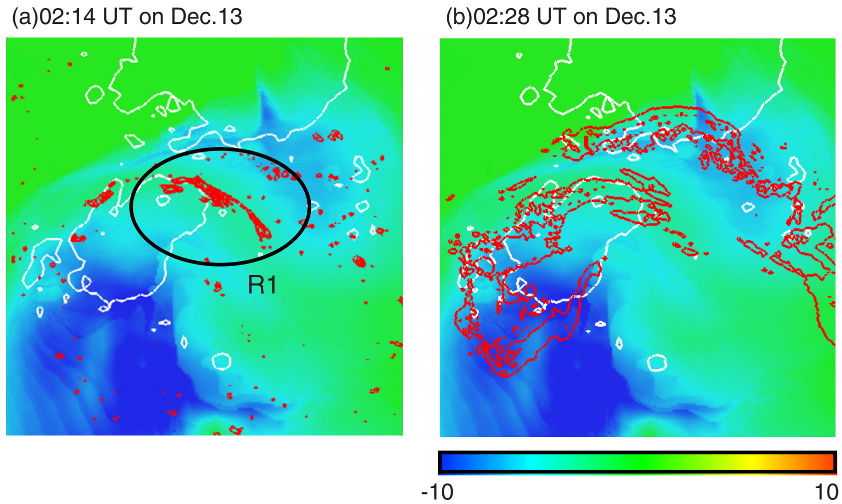

Figure 8. Contour of Ca II (red lines) intensity and the normal component of the positive (790 G) and negative (−790 G) magnetic fields (white lines) are plotted on the LOS-integrated twist. A difference between (a) and (b) is the observation time of the Ca II image. (a) shows the initial brightening phase of Ca II at 02:14 UT on December 13 and (b) the growing phase of the two-ribbon flare at 02:28 UT on December 13.

(A color version of this figure is available in the online journal.)

contour corresponds to the region of a strong X-ray intensity of more than 6.8. The regions named as IR1 and OR1 represent an inner or outer region surrounded by the red contour. We clearly see that the field lines of small length occupy most of the IR1 region while most of the OR1 is occupied by longer field lines. According to Figure 7, the brighter region in the soft X-ray corresponds to the region of the shorter field lines. This can be explained by the fact that it is not easy to heat the whole plasma contained in longer field lines as compared to shorter ones. From this study, the twist value has no direct relation with X-ray emission, because the twist value is more sensitive to the loop length from Equation (7) rather than the strong shear on their footpoints.

4.2. *Formation of the Sigmoid*

We compare the NLFFF with theoretical models derived from the kink instability and flux emergence. The purpose of this investigation is to clarify the origin of the sigmoid. Although the photospheric motions (twist or shear) are also able to generate the sigmoidal field lines and current structure, these motions are widely believed to be derived from a flux emergence. Moreover, the shear and twist motions are also accompanied with the flux-emergence motion, as reported comprehensively in several numerical studies (Magara 2006; Manchester 2008; Fan 2009). Therefore, in this study, we focus on the two formation processes for the formation of the sigmoid, known as kink instability and flux emergence.

4.2.1. *Sigmoid Formation from Kink Instability*

A kink instability may be one of the candidates to generate a sigmoidal current structure under an eruptive flux tube as noted from the numerical studies of Kliem et al. (2004), Fan & Gibson (2004), and Inoue & Kusano (2006). For the chosen AR (which is under consideration in this study), Inoue et al. (2011) have already indicated that the twist value obtained from this NLFFF is not enough to cause a kink instability. In this study, we further plotted the Ca II images of the initial (at 02:14 UT on December 13) and growth phase (at 02:28 UT on December 13) of the two-ribbon flare over the LOS-integrated twist map as shown in Figures 8(a) and (b), respectively. An initial strong illumination of Ca II begins to brighten at the R1 region marked by the solid circle in Figure 8(a). The twist value on this region is much smaller than the outer region. Therefore, the trigger of the solar flare is derived from the less twisted field lines which are not efficient enough to cause the kink instability. On the other hand, in the growth phase, the contours of the strong illumination of Ca II correspond to the strong twist region. From this result, it is evident that the elbow part of the sigmoid seems to play an essential role releasing the main magnetic energy rather than triggering the AR. Details about the triggering processes will be summarized in the next paper.

4.2.2. *Sigmoid Formation from Flux Emergence*

Next, we compare the NLFFF with a sigmoidal structure from a flux-emergence simulation performed by Magara (2004), which assumes a simple solution that an ideal helical flux tube embedded in the convection zone emerges to the no pre-existing coronal field through the photosphere and forms coronal magnetic loops. Figures 9(a) and (b) represent the selected field lines on the field-aligned current distribution map at about 1000 km above the photosphere from their simulation. The gray colored lines connect the strong field-aligned current regions ($|J_{\rm FAC}| > 7.5$). On the other hand, the orange field lines are traced from the regions t1 and t2 where the field-aligned current is a little weaker ($|J_{\rm FAC}| \approx 7.5$) than the region of the footpoints of the gray field lines and surrounding the gray color lines. This situation is similar to the NLFFF in that the central part of the sigmoid is distributed in the strong field-aligned current region while the footpoints of the field lines composing the elbow part of the sigmoid are distributed in the weaker field-aligned current region.

We also estimate the twist value of these field lines and compare them with that of NLFFF. In this case, the average force-free parameter $\bar{\alpha}$ is focused on the region where the normal component of the magnetic field (B_z) exceeds 0.1 (the maximum $|B_z| = 1.0$ at about 1000 km above the photosphere) and the other area is α_+(or α_-) $= 0$ to avoid the numerical noise. We also operate the averaging over 3×3 cells on α_+ and α_-.

Figure 9(c) shows the twist distribution mapped on the surface at 1000 km above the photosphere. Because the initial state of

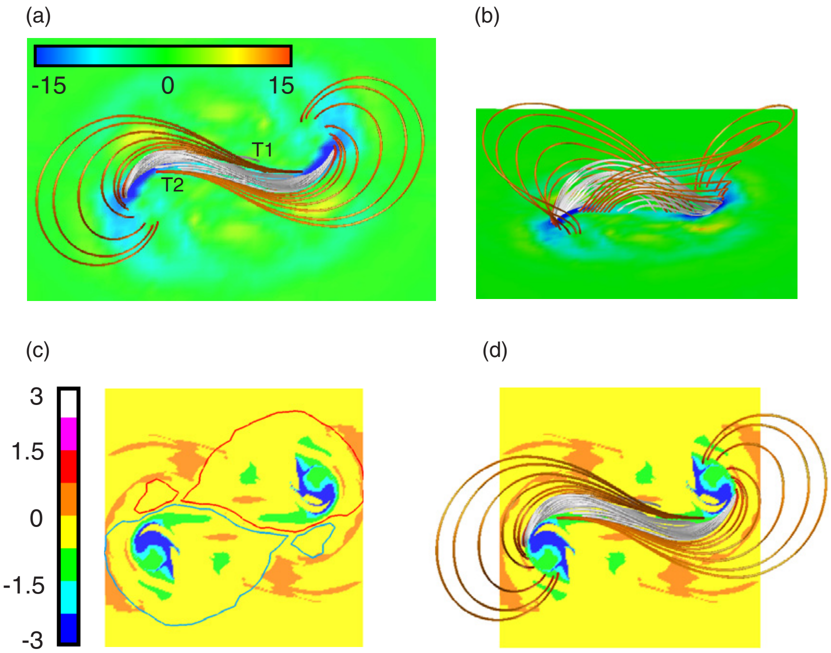

Figure 9. These results are obtained from the flux-emergence simulation by Magara (2004). (a) Field lines are plotted on the field-aligned current density map. The gray field lines connect the strong field-aligned current regions and orange field lines, whose footpoints are distributed on the relatively weak field-aligned current and surrounding the gray field lines (b) A side view of (a). (c) The twist obtained from Magara (2004) is mapped on the surface at 1000 km above the photosphere. The red and blue lines represent the contours of the normal component of the positive and negative magnetic fields. (d) The field lines are the same format as (a) and (b) and are plotted on the twist map in (c).

(A color version of this figure is available in the online journal.)

the numerical simulation is assumed by the left-handed flux tube embedded in the convection zone, the emerging loops mostly take the negative twisted distribution. The red and blue contours represent the normal component of the positive and negative magnetic fields. The field lines in Figures 9(a) and (b) are plotted over the twist map in Figure 9(d). This result clearly shows that all the field lines, which are composed of a sigmoid, plotted in Figure 9 are distributed in the twist range from $0.75 < |Tn| < 1.5$, which is a little larger than that from NLFFF.

Figures 1(a) and (b) also represent the 3D field lines whose different colors indicate the different twisted values. The purple and orange colors represent the twist range from $2.25 < |T_n|$ and $0.75 < |T_n| < 1.5$, respectively. The thick red and yellow lines indicate the magnetic axis and U-loop structure pointed out by Magara (2004). These lines are also included in the range of $0.75 < |Tn| < 1.5$. We also clearly see that the inverse S-shaped structure is well captured by the orange field lines and the U-loop. On the other hand, the purple field lines with a strong twist ($|T_n| > 2.25$) seem to form an S-shaped structure that is opposite to the orange and yellow field lines. Furthermore, we clearly see that the purple field lines rise to a higher position than the flux tube axis and other field lines. Magara (2004) had already pointed out that these purple lines above the flux tube axis take the continuous emergence from an initial phase and do not allow the chirality rule of the sigmoid. Therefore, these twist analyses suggest that the field lines constructing the sigmoid are mainly orange field lines and U-loop structures whose twisted values take a range of $0.75 < |Tn| < 1.5$. Our NLFFF reproduced the short field lines distributed in the strong field-aligned current region in the central part of the sigmoid. Unfortunately, the U-loop described by the thick line in Figures 1(a) and (b) cannot be reproduced in our NLFFF, which is actually in a fairly dynamic state in the simulation.

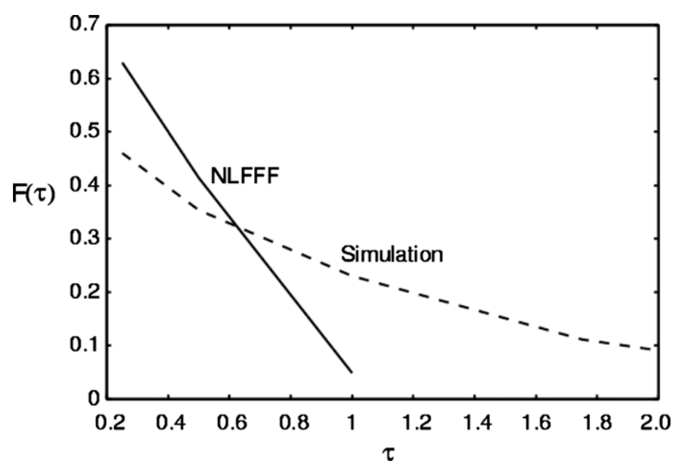

Figure 10. Profile of the $F(\tau)$, which is the fraction of the magnetic flux twisted more than τ to the total flux integrated over the region in the display size of Figure 4(b) (NLFFF) and Figure 9(c) (flux-emergence simulation). $F(\tau)$, determined by NLFFF and the flux-emergence simulation performed by Magara (2004), are plotted by the solid and dashed lines, respectively.

Finally, we quantitatively compare the twisted field lines of NLFFF with a result of the simulation. We define the equation to estimate the ratio of the magnetic flux twisted more than a critical twist τ to the total magnetic flux:

$$F(\tau) = \frac{\int_{|T_n|>\tau} B_z dS}{\int B_z dS}, \tag{10}$$

where the surface integral is taken on the positive pole $B_z > 0$ in the region. The $F(\tau)$ in the NLFFF case is calculated in the display size of Figures 4(a) and (b). On the other hand, for the case of the flux-emergence simulation it is done in the display size of Figure 9(c). The solid and dashed lines in Figure 10 show the F profiles of NLFFF for the AR 10930 and flux-emergence simulation to the critical vale τ. We clearly see that the F profile of NLFFF decreases compared with the simulation result as τ increases. When τ reaches about 0.65, the F value is almost the same. A gradual change of F in the simulation might depend on the profile of the magnetic field assumed for a flux tube, that is, the Gold-Hoyle flux tube used in the simulation is composed of field lines twisted in various ways so the magnetic structure formed by the flux tube also has a wide range of τ value. In fact, NLFFF does not reproduce the strongly twisted field lines as the numerical simulation does.

5. SUMMARY

In this study, we extrapolated a 3D coronal magnetic field in AR 10930 under the NLFFF approximation and investigated the 3D sigmoidal structure and associated twist value of the field lines. We also investigated a relationship between the field-aligned current flowing in the chromospheric region and the field lines composing a sigmoid. As a result, a sigmoid is constructed by the multiple sheared loops of various twist values. The elbow part of the sigmoid is composed of the higher twisted lines about $0.5 < |T_n| < 1.0$, while the central part is occupied by the less twisted lines $|T_n| < 0.5$. The field-aligned current distribution, however, is noticed in the opposite sense that the central part is stronger than the elbow part. As the less twisted lines are composed of the shorter field-line length, so the plasma contained in the shorter field lines is well heated through the derived strong field-aligned current on their footpoint and, as a result, strong X-ray emission is obtained from the central part of the sigmoid.

The twist value of the field lines obtained from Magara (2004) was also estimated and compared with NLFFF. The twist of the field lines obtained from the numerical simulation for the sigmoidal structure is $0.75 < |T_n| < 1.5$, which is somewhat larger than the value obtained from NLFFF. The field lines of the central part of the sigmoid are shorter in length and connect the strong field-aligned current regions on their footpoints. Therefore, the plasmas frozen in these shorter field lines are expected to be effectively heated through the Joule heating on their footpoints. On the other hand, the field lines composing the elbow part of the sigmoid are relatively longer in length compared to the central part, and the weaker field-aligned current distribution is noticed in their footpoint. This situation is similar to NLFFF. From our results, the U-loop (the thick yellow line in Figures 1(a) and (b)) can undoubtedly capture the inverse S-shaped structure. Magara & Longcope (2001) proposed that it has an important role in producing a flare; the magnetic field of the U-loop is vertically stretched and forms a current sheet below the axis. The strong X-ray emission region may be located below the U-loop, where the gray field lines and orange field lines in Figure 9 exist. Here the strong electric current ($|J_{\rm FAC}| \geqslant 7.5$) flows at the chromospheric footpoints of the gray and orange field lines while the current ($|J_{\rm FAC}| < 3.0$) at the footpoint of the U-loop is relativity weak. However, we do not make a final conclusion without quantitatively analyzing an essential structure associated with the X-ray and EUV emission as, e.g., Mok et al. (2005, 2008), Lionello et al. (2009), and Downs et al. (2010).

Furthermore, as we were not able to confirm this U-loop like structure (the thick yellow line in Figures 1(c) and (d)) in NLFFF, this result suggests that NLFFF can reproduce only up to a part lower than the location of U-loop formation. A detailed NLFFF reconstruction of the flux-emergence region is a future task.

We also noted that the all flux-emergence regions do not always generate the sigmoid structure. A flux tube cannot form a sigmoid if the twist of the flux tube is too weak, as suggested by Magara (2006). Their result also showed the much different current distribution between highly and weakly twisted cases. We do not know yet whether NLFFF can apply to the weak field region or not. If the magnetic field is strongly distorted by the plasma convection through an emerging process, NLFFF may not be efficient to reproduce the weak field regions.

Finally, we would like to say that the present study quite comprehensively explains one of the observed sigmoids, it does not mean it would be efficient to explain several other sigmoids. The magnetic structure of an evolving sigmoid using force-free modeling will also give important insight into the origin of a sigmoid followed by a flare. In this respect, *Hinode* has successfully obtained a time series of vector-field maps of the photospheric field in AR 10930 where an X3.4 class flare occurred. In a future work, we will use them to investigate the evolution of the magnetic field in this AR and will address the issue of the possible mechanism of solar flares.

S.I. thanks Dr. Y. Morikawa and the informatics project team in the Space Weather and Environment Informatics Laboratory in NICT for supporting our research. S.I. is also grateful to the anonymous referee for their constructive comments and Dr. Vinay Shankar Pandey for reading the draft paper. This work was supported by the Grant-in-Aid with an incentive study of the NICT's president fund. This research was also supported by the WCU (World Class University) program (R31-10016) through the National Research Foundation of Korea as well as the Basic Science Research Program (2010-0009258, PI: T. Magara). The ambiguity resolution code used herein was developed by K. D. Leka, G. Barnes, and A. Crouch with NWRA support from SAO under NASA NNM07AB07C. *Hinode* is a Japanese mission developed and launched by ISAS/JAXA, with NAOJ as a domestic partner and NASA and STFC (UK) as international partners. It is operated by these agencies in cooperation with ESA and NSC (Norway). The computational resources, data analysis, and visualization system were done by the Cybermedia Center at Osaka University, and by using resources from the OneSpaceNet in the NICT Science Cloud.

REFERENCES

Archontis, V., Hood, A. W., Savcheva, A., Golub, L., & Deluca, E. 2009, ApJ, 691, 1276
Aulanier, G., Török, T., Démoulin, P., & DeLuca, E. E. 2010, ApJ, 708, 314
Canfield, R. C., Hudson, H. S., & McKenzie, D. E. 1999, Geophys. Res. Lett., 26, 627
Downs, C., Roussev, I. I., van der Holst, B., et al. 2010, ApJ, 712, 1219
Fan, Y. 2009, ApJ, 697, 1529
Fan, Y., & Gibson, S. E. 2004, ApJ, 609, 1123
He, H., Wang, H., & Yan, Y. 2011, J. Geophys. Res. (Space Phys.), 116, 1101
Inoue, S., & Kusano, K. 2006, ApJ, 645, 742
Inoue, S., Kusano, K., Magara, T., Shiota, D., & Yamamoto, T. T. 2011, ApJ, 738, 161
Inoue, S., Kusano, K., Masuda, S., et al. 2008, in ASP Conf. Ser. 397, First Results From Hinode, ed. S. A. Matthews, J. M. Davis, & L. K. Harra (San Francisco, CA: ASP), 110
Inoue, S., & Morikawa, Y. 2011, Plasma Fusion Res., 6, 2401067
Kliem, B., Titov, V. S., & Török, T. 2004, A&A, 413, L23
Kosugi, T., Matsuzaki, K., Sakao, T., et al. 2007, Sol. Phys., 243, 3
Kusano, K. 2005, ApJ, 631, 1260
Leamon, R. J., Canfield, R. C., Blehm, Z., & Pevtsov, A. A. 2003, ApJ, 596, L255

Leka, K. D., Barnes, G., & Crouch, A. 2009, in ASP Conf. Ser. 415, The Second Hinode Science Meeting: Beyond Discovery-Toward Understanding, ed. B. Lites, M. Cheung, T. Magara, J. Mariska, & K. Reeves (San Francisco, CA: ASP), 365
Lionello, R., Linker, J. A., & Mikić, Z. 2009, ApJ, 690, 902
Magara, T. 2004, ApJ, 605, 480
Magara, T. 2006, ApJ, 653, 1499
Magara, T., & Longcope, D. W. 2001, ApJ, 559, L55
Magara, T., & Longcope, D. W. 2003, ApJ, 586, 630
Manchester, W. 2008, in ASP Conf. Ser. 383, Subsurface and Atmospheric Influences on Solar Activity, ed. R. Howe, R. W. Komm, K. S. Balasubramaniam, & G. J. D. Petrie (San Francisco, CA: ASP), 91
Manchester, W., IV, Gombosi, T., DeZeeuw, D., & Fan, Y. 2004, ApJ, 610, 588
Matsumoto, R., Tajima, T., Chou, W., Okubo, A., & Shibata, K. 1998, ApJ, 493, L43
McKenzie, D. E., & Canfield, R. C. 2008, A&A, 481, L65
Mok, Y., Mikić, Z., Lionello, R., & Linker, J. A. 2005, ApJ, 621, 1098
Mok, Y., Mikić, Z., Lionello, R., & Linker, J. A. 2008, ApJ, 679, L161
Moore, R. L., Sterling, A. C., Hudson, H. S., & Lemen, J. R. 2001, ApJ, 552, 833
Rust, D. M., & Kumar, A. 1996, ApJ, 464, L199
Rust, D. M., & LaBonte, B. J. 2005, ApJ, 622, L69
Savcheva, A., & van Ballegooijen, A. 2009, ApJ, 703, 1766
Schrijver, C. J., DeRosa, M. L., Metcalf, T., et al. 2008, ApJ, 675, 1637
Sterling, A. C., & Hudson, H. S. 1997, ApJ, 491, L55
Su, Y., van Ballegooijen, A., Lites, B. W., et al. 2009, ApJ, 691, 105
Titov, V. S., & Démoulin, P. 1999, A&A, 351, 707
Török, T., & Kliem, B. 2003, A&A, 406, 1043
Tsuneta, S., Hara, H., Shimizu, T., et al. 1992, PASJ, 44, L63